# Analysis and fast modelling of microstructures in duplex stainless steel formed by directed energy deposition additive manufacturing

Alexander Edwards, Daniel Weisz-Patrault, Éric Charkaluk

# Highlights

**Analysis and fast modelling of microstructures in duplex stainless steel formed by directed energy deposition additive manufacturing**

Alexander Edwards, Daniel Weisz-Patrault, Éric Charkaluk

- Duplex stainless steel has been fabricated by laser metal powder directed energy deposition.
- A microstructural analysis revealed a gradient of austenite phase fraction as a function of distance from the build platform.
- A fast numerical approach has been developed to model both temperature kinetics, grain size during solidification and diffusion controlled phase transition as a function of process parameters.
- Satisfying agreement with the experimental data is observed.
- Temperature control of the build platform is proposed to reach more uniform and balanced ferrite to austenite phase ratios.

# Analysis and fast modelling of microstructures in duplex stainless steel formed by directed energy deposition additive manufacturing

Alexander Edwards[a], Daniel Weisz-Patrault[a], Éric Charkaluk[a]

[a]*École Polytechnique, Institut Polytechnique de Paris, LMS, CNRS, F-91128 Palaiseau, France*

**Abstract**

The properties of duplex stainless steels depend strongly on their thermal history, which can produce a wide range of austenite to ferrite ratios; whereas optimal properties generally require near 50-50 ferrite-austenite duplex microstructures. Additive manufacturing processes of duplex steels remain challenging as it is difficult to predict and control how the phase ratio depends on process parameters. This paper focuses on directed energy deposition additive manufacturing and presents a fast numerical modelling of the thermal history and diffusion controlled solid-solid phase transformations in the entire part. The proposed simulations strategy is sufficiently fast to optimize the process parameters to achieve a targeted distribution of phase ratio, and a temperature control strategy of the build platform has been proposed on this basis to reach almost uniform near 50-50 phase ratios, which was obtained by setting the temperature profile of the build platform as a linear function decreasing from 1000 K for the first layer to 800 K for the last layer. In addition, experiments are conducted to validate the proposed approach. Microstructures and phase ratio gradients are assessed in single-bead-thickness walls of SAF 2507 superduplex stainless steel, and numerical results are in reasonable agreement with experimental observations.

*Keywords:* Duplex steel, Directed Energy Deposition, Microstructure, Phase gradients

## 1. Introduction

Significant progress in additive manufacturing (AM) technologies, have taken place over the last decade. However, applications are restricted by the unpredictability of the product properties, as porosity, microstructure and residual stresses, which all depend on product geometry and processing parameters. Therefore it is essential to develop realistic numerical models that can predict, and so control, these properties. Directed energy deposition (DED) is a form of additive manufacturing (AM) in which a heat source melts extra material layer by layer onto a built platform (i.e., substrate). In laser metal powder directed energy deposition (LMPDED), metal powder is fed coaxially with a laser. As shown in figure 1, the powder is transported by a cover gas through the nozzle to the build platform, where it is melted by the laser to form a melt pool. The nozzle moves parallel with the substrate in order to form beads of metal alloy. Each bead can act as a foundation for subsequent beads, building the final product layer by layer.

∗Corresponding author: *daniel.weisz-patrault@cnrs.fr*

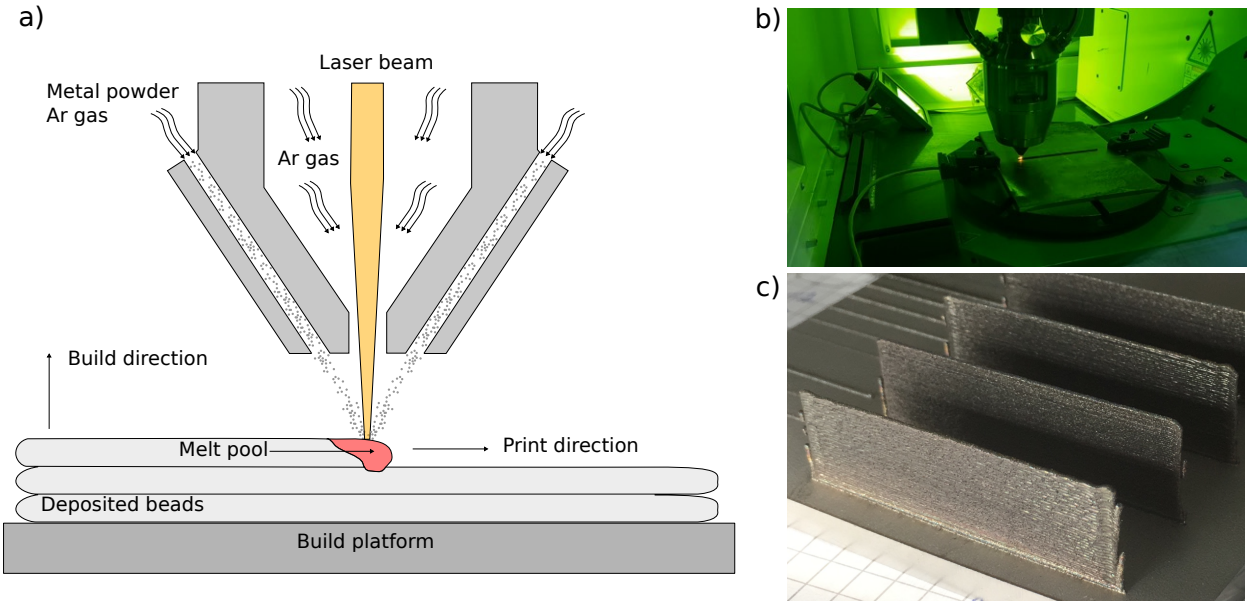


Figure 1: a) Schematic representation of laser metal powder directed energy deposition. This figure is inspired by Lim et al. [1], b) picture of the LMPDED process, c) thin walls in 2507 DSS.

Because of the complex thermal history non-uniform solid-state phase transitions are obtained [2], and the application of DED to duplex stainless steels (DSS) has therefore been limited by the inability to form a uniform and balanced ferrite/austenite microstructure in the as-printed material, which is essential to ensure their properties [3]. For this reason, there are only a few papers on AM of DSS [4] in the literature. Laser powder bed fusion (LPBF), wire arc additive manufacturing (WAAM), and directed energy deposition (DED) with wire or powder have been tested, and a wide range of phase ratios in as-printed specimens are reported: from almost fully ferritic microstructure using LPBF [5–7] to up to 38vol% austenite microstructure for LMPDED [8], and 80vol% for WAAM [9, 10] depending on the typical cooling rates associated with each technology. In addition, the non-uniformity of the phase ratio in DED is pointed out in [11] where the austenite fraction increased with distance from the substrate: from 55vol% at 5-10 mm to 70vol% at 20 mm. A balanced and more uniform austenite/ferrite ratio could be achieved by subsequent annealing at around 1400 K [5, 6]; however, not only is this an additional manufacturing step which can lead to dimensional changes, but in some important applications, such as repair of existing components, it is impossible.

Considering these difficulties, a natural idea is to simulate the AM process and phase transition so that the process parameters can be optimized in order to reach a targeted phase fraction ratio. Regarding numerical approaches to compute temperature fields in LMPDED, many papers focus on very detailed simulations at the mesoscopic scale, especially powder melting, the hydrodynamic problem, and crystallization during cooling (e.g., [12–14]). However, such numerical simulations are often limited to a single layer, and cannot capture phase gradients in the entire part. Macroscopic simulations have also been developed (e.g., [15–17]) but are still computationally costly. Thus, simplified linear thermal analyses have been proposed (e.g., [18, 19]), which neglect the latent heat

of fusion, and are limited to simple flat-wall geometries. In this paper, a fast numerical approach [20, 21], which can deal with more complex geometry and takes account of latent heat release during solidification, is used. This approach to temperature modelling has already been validated experimentally by infrared measurements using a pyrometer [20] and an infrared camera [22], and was used to predict residual stresses [22] and grain growth [23–25].

In the literature, the ferrite to austenite phase transition in DSS has been modeled in different ways. For instance, Johnson-Mehl-Avrami equation has been fitted on experiments [26, 27]. However, DED is characterized by complex thermal cycling, so a diffusion controlled growth model is preferable to estimate austenite growth, which takes place from the grain boundaries (GB) and depends on ferrite grain size. Diffusion controlled growth theories [28–31] usually involve to solve a 1D diffusion problem in an infinite or a finite slab with mass conservation in the grain (i.e., no mass exchange with other grains) under the assumption that the composition of ferrite and austenite at their mutual interface is in local equilibrium. It should be noted that this equilibrium condition makes sense as the interface during solid-state phase transition evolves rather slowly, and is only assumed locally at the interface, which authorizes non-equilibrium diffusion in solid phases.

The $\delta$ ferrite to $\gamma$ austenite phase transition is initially assisted by fast diffusion of N (i.e., strong austenite stabilizer by weight), then when the temperature decreases a slower diffusive mechanism takes place involving Cr (i.e., ferrite stabilizer), which diffuses from austenite to ferrite, and Ni (i.e., austenite stabilizer), which diffuses from ferrite to austenite. This diffusive mechanism limits the phase transition rate, because both Cr and Ni are substitutionally-diffusing elements, which diffuse orders of magnitude slower than interstitial elements such as N. Both Cr and Ni could have been taken into account together in the diffusion problem below 1587 K, but only Ni has been considered as Ni and Cr share similar diffusive properties. Thus, the phase transition is computed by solving a two-species diffusion problem (i.e., N and Ni).

The diffusion controlled phase transition model directly involves the grain size, which should therefore be estimated as a function of solidification conditions. Of course, phase-field models [32], cellular automaton [33] or a combination of both [34] could be used to obtain the detailed grain structure under additive manufacturing conditions. But such models are time consuming and it would be counterproductive to estimate only the grain size of such detailed simulations. In the literature, several other faster approaches have been proposed to determine the grain size, and some of them have been applied to additive manufacturing conditions [35]. Common approaches involve nucleation of dendritic equiaxed grains from preexisting impurities [36], whose distribution is unknown, which limits their applicability within the framework of the present work. A simpler empirical approach [37] enabling to relate the grain size and the cooling rate during solidification in the form of a power law is preferred.

This paper aims at developing a fast numerical simulation of temperature and diffusion controlled ferrite to austenite phase transition of DSS obtained by DED in order to determine process parameters and temperature control systems enabling to reach a targeted microstructure, namely a rather uniform and balanced ferrite/austenite ratio. The proposed model is validated on experiments, which assess the microstructures and proportion of austenite to ferrite in single bead thickness walls of SAF 2507 super-duplex stainless steel obtained via LMPDED.

The paper is organized as follows. The experimental study is presented in section 2. Theoretical developments are presented in section 3. The thermal analysis proposed in [20] is used and some

improvements are proposed. In addition, a fast diffusion-controlled growth model based on semi-analytical developments is derived. The composition at the austenite/ferrite interface is assumed to be at equilibrium, therefore an equilibrium computation has been carried out with Thermo-Calc [38], which is used as inputs for the diffusion model. Results are presented in section 4, and a comparison between experiments and numerical computation is provided. In addition, the effect on the ferrite to austenite ratio of preheating the substrate or even control its temperature during fabrication is investigated in section 5. Conclusive remarks are given in section 6.

## 2. Materials and method

Two experiments have been conducted on SAF 2507 DSS walls built via DED using a BeAM Mobile-004 machine equipped with a Itterbium YLR fibre laser (1070 nm wavelength) and a 500 W maximum power output. The walls were constructed using a powder feedstock of SAF 2507 DSS made by Sandvik, with a 77.6 µm average powder particle diameter and 98.4% of particles in the range of 45-99 µm. The composition was verified by Sandvik and corresponded to the SAF 2507 DSS norms and a scanning electronic microscope characterization of powder is provided in figure 2. The nominal powder composition is given in table 1.

Table 1: Nominal DSS Alloy Composition SAF 2507 DSS in wt%

| Fe | Ni | Cr | Mo | Mn | N | C | Si | P | Cu | S |
|---|---|---|---|---|---|---|---|---|---|---|
| Balance | 7 | 25 | 4 | 1.2 | 0.285 | 0.03 | 0.8 | 0.035 | 0.5 | 0.02 |

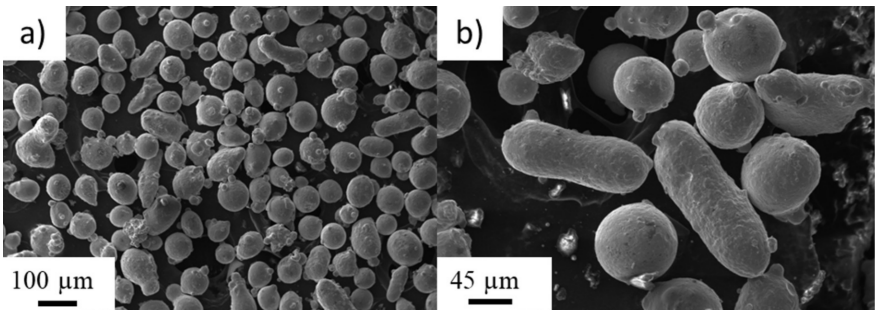


Figure 2: SEM observation of the powder.

The two walls were built to single bead thickness. No dwell time was applied and the printing direction alternated between layers. The printing was carried out using the DSS powder starting on a 316 austenitic stainless steel build platform. The length of the wall was set to 50 mm along the print direction $X$. The height was controlled by the increment between layers (0.16 mm) along the build direction $Z$, and the number of layers, which was adjusted to achieve around 16 mm of wall height from the substrate (100 layers). The printing speed was 2000 mm.min$^{-1}$, with 7.1 g/min powder flow, and 225 or 250 W laser power for experiment 1 and 2 respectively. All process parameters are listed in table 2. These process parameters have been selected based on previous

computations and experiments. In particular the fabrication is stopped after 100 layers to avoid buckling [22], and the substrate thickness is chosen so that no significant distortions take place. The laser speed, scanning strategy, dwell time and laser powers are chosen so that the accumulated heat enables to transform enough austenite [20].

Table 2: Simulation parameters

| | | | |
|---|---|---|---|
| Number of layers | $N_{\text{lay}}$ | (-) | 100 |
| Substrate thickness | $h_{\text{sub}}$ | (mm) | 5 |
| Initial substrate temperature | $T^0_{\text{sub}}$ | (K) | ∼300 |
| Length of wall | $L$ | (mm) | 50 |
| Powder flow | $Q_{\text{flow}}$ | (g.min$^{-1}$) | 7.1 |
| Layer height | $h_z$ | (µm) | 160 |
| Layer thickness | $h_y$ | (µm) | 650 |
| Laser beam radius | $R_{\text{beam}}$ | (µm) | 338 |
| Laser beam speed | $V_{\text{beam}}$ | (mm.min$^{-1}$) | 2000 |
| Dwell time | $t_{\text{dwell}}$ | (s) | 0 |
| Laser beam power | $P_{\text{beam}}$ | (W) | 250 (resp. 225) |

The printed walls were then cut along the plane perpendicular to the print direction to extract cross section samples. The section taken from the as-printed duplex steel wall is illustrated in figure 3. The red highlighted area represents the surface area where the microstructure is analysed. These samples were then set in conducting epoxy resin and polished. Polishing was carried out using grinding paper down to P4000 (5 µm), then diamond paste polishing with 3 µm, followed by 1 µm. The final polishing step consisted of ion polishing using 6 kEV, 6 rpm and an incident angle of 6 degrees. The microstructures of the samples were analysed in a scanning electron microscope (SEM) using electron backscatter diffraction (EBSD) in a Quanta 600 with a detector which enables maximum frame rate of 3000 Hz.

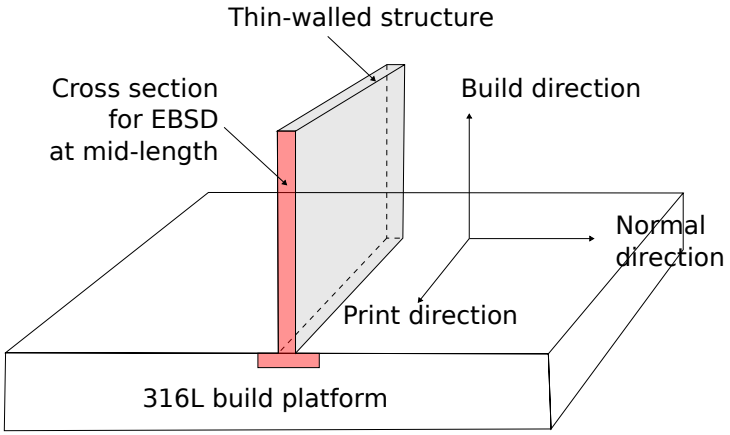


Figure 3: Illustration of the section of the wall, with the EBSD map area highlighted in red.

## 3. Theory

### *3.1. Temperature field computation*

The computation of the temperature field relies on the assumption that for single bead structures, heat fluxes along the print direction are negligible with respect to the build and normal directions. Based on this assumption a numerical strategy has been established in [20] based on analytical solutions of successive 2D multilayer composites heat conduction problems. Three improvements are proposed in this contribution to better capture the $\delta \rightarrow \gamma$ phase transition. First, the deposition temperature denoted by $T_{\text{dep}}$ is a parameter corresponding to the melt pool temperature, and has been calibrated for specific process parameters. In this contribution, since two experiments have been performed with two different laser power, the deposition temperature is approximated as in [22] by the following analytical form [39]:

$$T_{\text{dep}} = \frac{I\,\eta\,R_{\text{beam}}}{\sqrt{2\pi}\lambda_{\text{liq}}}\arctan\left(\frac{\sqrt{8\,D_{\text{liq}}t_{\text{beam}}}}{R_{\text{beam}}}\right) \tag{1}$$

Where $R_{\text{beam}}$ is the laser beam radius defined as two standard deviations of the Gaussian laser distribution, $\lambda_{\text{liq}}$ and $D_{\text{liq}}$ are respectively the thermal conductivity and diffusivity of the liquid metal, $I = 2\,P_{\text{beam}}/(\pi R_{\text{beam}}^2)$ is the laser intensity, $\eta$ is the absorptivity of the powder, and $t_{\text{beam}} = \sqrt{2}\,R_{\text{beam}}/V_{\text{beam}}$ with $V_{\text{beam}}$ the laser beam velocity.

The second improvement is related to the latent heat of fusion. Indeed, the latent heat of fusion was taken into account in [20] by interpolating the liquid to solid phase transition rate on a series of time decreasing exponential functions. However, the heat source due to the phase transition does not start immediately after the deposition of the molten metal, but only when the temperature reaches the liquidus temperature $T_{\text{liq}}$. This delay being difficult to capture with time decreasing exponential functions, the heat source was applied at $t = 0$ directly when the molten metal was deposited. If this approximation is acceptable to capture the temperature kinetics of the solid material, the cooling rate during solidification cannot be estimated accurately. As detailed in the following, the studied $\delta \rightarrow \gamma$ phase transition depends on the grain size of the solidified $\delta$ phase, which highly depends on the cooling rate during solidification. Therefore, the approach proposed in [20] has been improved to correctly address the cooling rates during solidification. To do so, a new initial condition is set at $t = t_{\text{liq}}$ when $T = T_{\text{liq}}$ (where $t$ denotes the time and $T$ the computed temperature), and the heat source due liquid to solid phase transition is applied.

The third improvement is related to the build platform temperature, which has a significant impact on the temperature kinetics. The substrate temperature was assumed to be constant and homogeneous during the fabrication of each layer, which is acceptable after a certain number of layers when the laser is sufficiently far from the substrate, but rather inaccurate for the first layers. To better capture the non-uniform distribution of phase fraction along the build direction, a better estimation of the substrate temperature is proposed in this paper by solving the following non-uniform 1D heat conduction problem:

$$\frac{\partial T_{\text{sub}}^n}{\partial t}(Z,t) - D_{\text{sub}}\frac{\partial T_{\text{sub}}^n}{\partial Z^2}(Z,t) = 0 \tag{2}$$

Where $T^n_{\text{sub}}$ is the substrate temperature during deposition of the $n$-th layer, $t$ the time, $Z$ the spatial coordinate along the print direction, and $D_{\text{sub}}$ ($\text{m}^2.\text{s}^{-1}$) the substrate thermal diffusivity. Boundary conditions read as convection conditions:

$$\begin{cases} -\lambda_{\text{sub}} \dfrac{\partial T^n_{\text{sub}}}{\partial Z}\left(\dfrac{h_{\text{sub}}}{2}, t\right) = H_{\text{build}}\left(T^n_{\text{sub}}\left(\dfrac{h_{\text{sub}}}{2}, t\right) - T^n_{\text{build}}\right) \\ \lambda_{\text{sub}} \dfrac{\partial T^n_{\text{sub}}}{\partial Z}\left(-\dfrac{h_{\text{sub}}}{2}, t\right) = H_{\text{plate}}\left(T^n_{\text{sub}}\left(-\dfrac{h_{\text{sub}}}{2}, t\right) - T_{\text{plate}}\right) \end{cases} \tag{3}$$

where $\lambda_{\text{sub}}$ ($\text{W.m}^{-1}.\text{K}^{-1}$) is the thermal conductivity of the substrate, $h_{\text{sub}}$ its thickness, $T^n_{\text{build}}$ is the average temperature of the bottom first layer of the part during the deposition of the $n$-th layer, $T_{\text{plate}}$ is the temperature of the plate beneath the substrate, and $H_{\text{build}}$ and $H_{\text{plate}}$ ($\text{W.m}^{-2}.\text{K}^{-1}$) are the heat transfer coefficients respectively between the part and the top surface of the substrate, and between the bottom surface of the substrate and the plate underneath. In addition the initial condition reads:

$$T_{\text{sub}}(Z, t = 0) = T^{n-1}_{\text{sub}}(Z, t^{n-1}) \tag{4}$$

where $T^{n-1}_{\text{sub}}(Z, t^{n-1})$ is the temperature of the substrate at the end of the previous layer deposition. The diffusion equation (2) with boundary conditions (3) and initial condition (4) is solved analytically in Appendix A. It should be noted that this approach is only meant to capture the average heat extracted from the part by the substrate, and crude assumptions have been made by neglecting heat flow in the substrate plane for instance. A better way to capture the substrate temperature would have been to add a thermocouple.

### *3.2. Diffusion controlled growth of austenite*

The phase transition is computed by solving a two-species diffusion problem. First the phase transition is controlled by the fast diffusion of N between 1602-1587 K, and then the phase transition is controlled by slower diffusion of Ni for lower temperatures. However, it should be noted that the diffusion of both N and Ni should be computed simultaneously so that the Ni concentration profile is estimated at 1587 K when Ni diffusion starts to control the phase transition. Since there is a large number of different layers subjected to thermal cycling, short computation time is obtained by developing a numerical strategy relying on analytical solutions of the diffusion equation. The proposed approach consists in solving the same diffusion problem as in [29–31] (i.e., mass balance in the grain and equilibrium at the $\delta/\gamma$ interface) in a 1D finite domain (i.e., sphere, cylinder or slab). However, the diffusion equation is highly non-linear due to the mobile $\delta/\gamma$ interface, and temperature dependant diffusivity and equilibrium phase fractions. To overcome this difficulty, a general analytical solution is derived for fixed $\delta/\gamma$ interface at constant temperature. Therefore, to correctly follow the phase transition evolution, a time discretization is introduced and the analytical solution is successively applied only during short time increments, which is consistent with the proposed assumptions (i.e., fixed $\delta/\gamma$ interface at constant temperature). In addition to temperature, the $\delta/\gamma$ interface is updated at the end of each time step based on the mass balance equation. Moreover, at each time step, a new initial condition is prescribed based on the solution concentration profile at the end of the previous time step. Of course, since between two successive time steps

the $\delta/\gamma$ interface is updated, the solution concentration profile is adapted to define the new initial condition in order 1) to be consistent with the new interface position and 2) to ensure that the total mass of the alloying element is unchanged.

The temperature dependant equilibrium concentrations of the alloying element in the $\delta$ and $\gamma$ phases are respectively denoted by $c^{\delta}_{\text{eq}}(T)$ and $c^{\gamma}_{\text{eq}}(T)$ (where $T$ (K) is the time dependent temperature). Moreover $w(t)$ (m) is the time dependant austenite thickness. The proposed strategy involves solving the following problem at each time step (indexed by $k$). The second Fick's law reads for 1D domains, $\forall t \in [t_k, t_{k+1}]$ (where $t_k$ is the time at the beginning of the $k$-th time step and $t_{k+1} = t_k + \Delta t_k$ where $\Delta t_k$ is the time increment):

$$\begin{cases} \dfrac{\partial c^{\delta}_k}{\partial t}(x,t) - \dfrac{D^{\delta}_k}{x^q}\dfrac{\partial}{\partial x}\left(x^q \dfrac{\partial c^{\delta}_k}{\partial x}(x,t)\right) = 0 & \text{if} \quad 0 \leq x \leq R - w_k \\ \dfrac{\partial c^{\gamma}_k}{\partial t}(x,t) - \dfrac{D^{\gamma}_k}{x^q}\dfrac{\partial}{\partial x}\left(x^q \dfrac{\partial c^{\gamma}_k}{\partial x}_{k}(x,t)\right) = 0 & \text{if} \quad R - w_k \leq x \leq R \end{cases} \tag{5}$$

Where for the time step $k$, $c^{\delta}_k(x,t)$ and $c^{\gamma}_k(x,t)$ are the concentration profiles of the considered alloying element (i.e., N and Ni) in the $\delta$ and $\gamma$ phases respectively, $D^{\delta}_k$ and $D^{\gamma}_k$ ($\text{m}^2.\text{s}^{-1}$) denote the diffusivity in the $\delta$ and $\gamma$ phases respectively, $w_k = w(t_k)$ (m) is the austenite thickness, $x$ denotes the spatial coordinate, and $q = 0, 1, 2$ for slab, cylinder and sphere respectively.

Boundary conditions read, $\forall t \in [t_k, t_{k+1}]$:

$$(a) \begin{cases} \dfrac{\partial c^{\delta}_k}{\partial x}(x = 0, t) = 0 \\ \dfrac{\partial c^{\gamma}_k}{\partial x}(x = R, t) = 0 \end{cases} \qquad (b) \begin{cases} c^{\delta}_k(x = R - w_k, t) = c^{\delta}_{\text{eq},k} \\ c^{\gamma}_k(x = R - w_k, t) = c^{\gamma}_{\text{eq},k} \end{cases} \tag{6}$$

It should be noted that $w_k$, $D^{\delta}_k$, $D^{\gamma}_k$, $c^{\delta}_{\text{eq},k}$, and $c^{\gamma}_{\text{eq},k}$ are assumed to be constant in $[t_k, t_{k+1}]$, and are only updated at the end of the time step. Equation (6) $(a)$ corresponds to mass conservation in the grain (i.e., no mass transfer outside the grain), and (6) $(b)$ corresponds to the equilibrium of the $\delta/\gamma$ interface.

The initial concentration profiles in the $\delta$ and $\gamma$ phases are respectively denoted by $c^{\delta}_{\text{ini},k}(x)$ and $c^{\gamma}_{\text{ini},k}(x)$, hence:

$$\begin{cases} c^{\delta}_k(x, t = t_k) = c^{\delta}_{\text{ini},k}(x) & \text{if} \quad 0 \leq x \leq R - w_k \\ c^{\gamma}_k(x, t = t_k) = c^{\gamma}_{\text{ini},k}(x) & \text{if} \quad R - w_k \leq x \leq R \end{cases} \tag{7}$$

At the beginning of diffusion (i.e., for the *first time step* $k = 1$ at $T = 1602$ K according to the ThermoCalc computation), the initial concentration profile of N is assumed to be uniform and equal to the bulk concentration in the $\delta$ phase, i.e., $c^{\delta}_{\text{ini},1}(x) = 0.29$wt% according to table 1. In addition, a nucleation thickness of the $\gamma$ layer is postulated and denoted by $w^{\gamma}_{\text{ini}}$, hence $w_1 = w^{\gamma}_{\text{ini}}$. The dimensionless normalized mass of N outside the ferrite bulk at 1602 K is extracted from the ThermoCalc computation and reads $m^{\gamma}_{\text{eq},N} = 1.598 \times 10^{-3}$ (g of N per g of compound), which is entirely affected to the nucleated layer of austenite, which reads $c^{\gamma}_{\text{ini},1}(x) = m^{\gamma}_{\text{eq},N}\, R/w^{\gamma}_{\text{ini}}$, where $R$ is the average equivalent grain radius. Furthermore, since Ni diffuses much slower, it is assumed that the initial concentration profile of Ni is uniform and equal to the bulk concentration in both the $\delta$ and $\gamma$ phases, i.e., $c^{\delta}_{\text{ini},1}(x) = c^{\delta}_{\text{ini},1}(x) = 7$wt% according to table 1.

For following time steps (i.e., $k \geq 2$) the initial concentration profile is based on the concentration at the end of the previous time step, which reads:

$$\begin{cases} c^{\delta}_{\mathrm{ini},k}(x) = \dfrac{c^{\delta}_{k-1}\left(\Lambda^{\delta}_{k}\, x, t = t_k\right)}{\Lambda^{\delta}_{k}} & \text{if} \quad 0 \leq x \leq R - w_k \\ c^{\gamma}_{\mathrm{ini},k}(x) = \dfrac{c^{\gamma}_{k-1}\left(\Lambda^{\gamma}_{k}\, x + \Gamma^{\gamma}_{k}, t = t_k\right)}{\Lambda^{\gamma}_{k}} & \text{if} \quad R - w_k \leq x \leq R \end{cases} \tag{8}$$

where:

$$\begin{cases} \Lambda^{\delta}_{k} = \dfrac{R - w_{k-1}}{R - w_k} \\ \Lambda^{\gamma}_{k} = \dfrac{w_{k-1}}{w_k} \qquad \text{and} \quad \Gamma^{\gamma}_{k} = R\left(\dfrac{w_k - w_{k-1}}{w_k}\right) \end{cases} \tag{9}$$

Where coefficients $\Lambda^{\delta}_{k}$, $\Lambda^{\gamma}_{k}$ and $\Gamma^{\gamma}_{k}$ have been introduced to accommodate the update of the austenite thickness $w_{k-1} \rightarrow w_k$, and to ensure that the total mass of the alloying element in the grain is conserved. The analytical solution of (5) with boundary conditions (6) and initial condition (7) is derived in details in Appendix B. Even though grains or sub-structures from which austenite is forming are close to spheres or cylinders, the analytical solution has been found to be much faster for slabs. Thus, the solution for slabs has been used in practise and the slab size has been adjusted to correspond to an equivalent sphere as detailed in Appendix B.

The update of the austenite thickness is obtained from mass balance, which reads:

$$\dot{w}(t) = D^{\delta}(T(t))\frac{\partial c^{\delta}}{\partial x}(R - w(t), t) - D^{\gamma}(T(t))\frac{\partial c^{\gamma}}{\partial x}(R - w(t), t) \tag{10}$$

Thus, the update is approximated as follows:

$$w_k = w_{k-1} + D^{\delta}_{k-1}\int_{t_{k-1}}^{t_k} \frac{\partial c^{\delta}_{k-1}}{\partial x}(R - w_{k-1}, t)\mathrm{d}t - D^{\gamma}_{k-1}\int_{t_{k-1}}^{t_k} \frac{\partial c^{\gamma}_{k-1}}{\partial x}(R - w_{k-1}, t)\mathrm{d}t \tag{11}$$

Where integrals are calculated analytically as detailed in Appendix B.

## 4. Results and discussion

### *4.1. Equilibrium computation*

Phase equilibria for 2507 duplex steel as a function of temperature were calculated using Thermo-Calc TCFE9 database using system conditions: pressure $10^5$ Pa, system size 1 mole, alloy composition according to table 1. The results of this equilibrium calculations are shown in figure 4. It provides the equilibrium concentration of alloying elements at different temperatures for the numerical simulation of solid-solid phase transformations. Starting from 1602 K, the top of the $\delta + \gamma$ phase region, as the temperature falls the equilibrium fraction of austenite increases and eventually becomes the majority phase (the 50-50 inflexion point is near 1400 K).

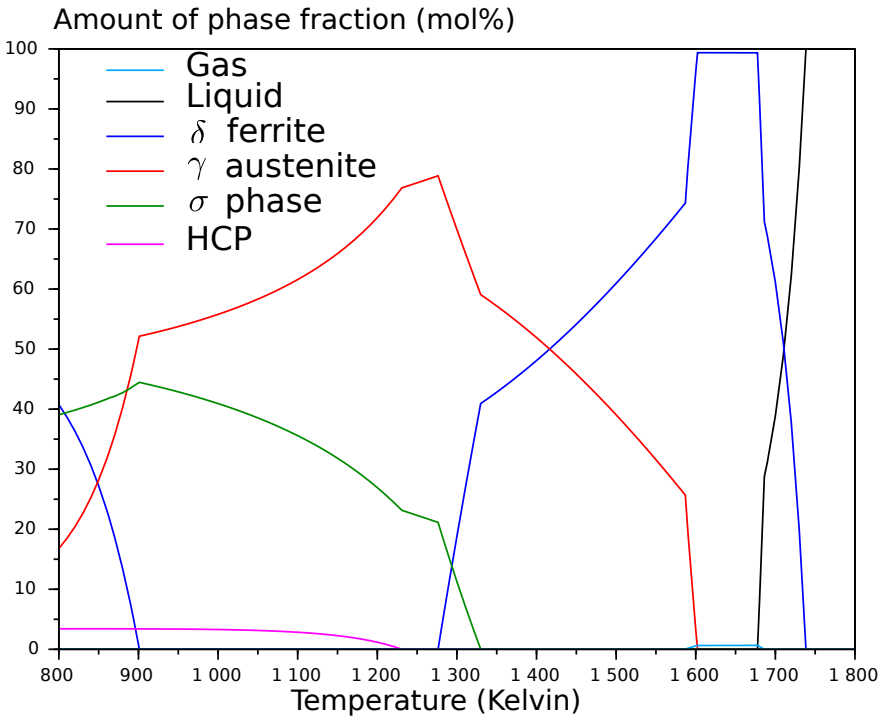


Figure 4: Diagram of phase fractions vs temperature for equilibria calculations using Thermo-Calc [38].

### *4.2. Experimental results*

The cross section taken from the as-printed duplex steel wall is illustrated in figure 3. The red highlighted area represents the surface area analysed by EBSD. In figure 5 (a) one can observe the distribution and form of austenite (red) and ferrite (blue) phases. Since super DSS is expected to solidify initially as ferrite, the distribution of austenite is mostly located along prior ferrite-ferrite GBs. Subsequent austenite growth also occurs into the existing grains of the ferrite matrix. The ferrite only EBSD inverse pole figure map of figure 5 (b) illustrates the morphology of the ferrite grains. The texture of these ferrite grains is analysed using pole figures in figure 6 which shows that in DSS the epitaxial ferrite grain growth follows predominantly the [100] direction [40]. The EBSD map can be broken down into 5 areas from left to right. One can observe that the 1-st and 5-th areas near the surface of the wall present negligible texture with equiaxed grains. In the second and fourth sections the epitaxial grains grow at an angle of approximately 35-45 degrees towards the centre following the [100] direction. Right in the middle the grain growth is no longer inclined with respect to the surface to the left or right, but rather towards the build direction (out of the page).

The grain size of the equiaxed grains within the first 100 µm of the wall surface is of the order of 10 µm. One expects to observe relatively small grains in duplex steel because austenite formed at the ferrite GBs inhibits the usual coarsening of ferrite grains by ferrite-ferrite GB mobility. The longer epitaxial grains that grow in from the wall surface show a wider range of sizes: they can grow even to 100 µm in length, but are on average 50 µm long, and 20 µm wide. An accurate measure of

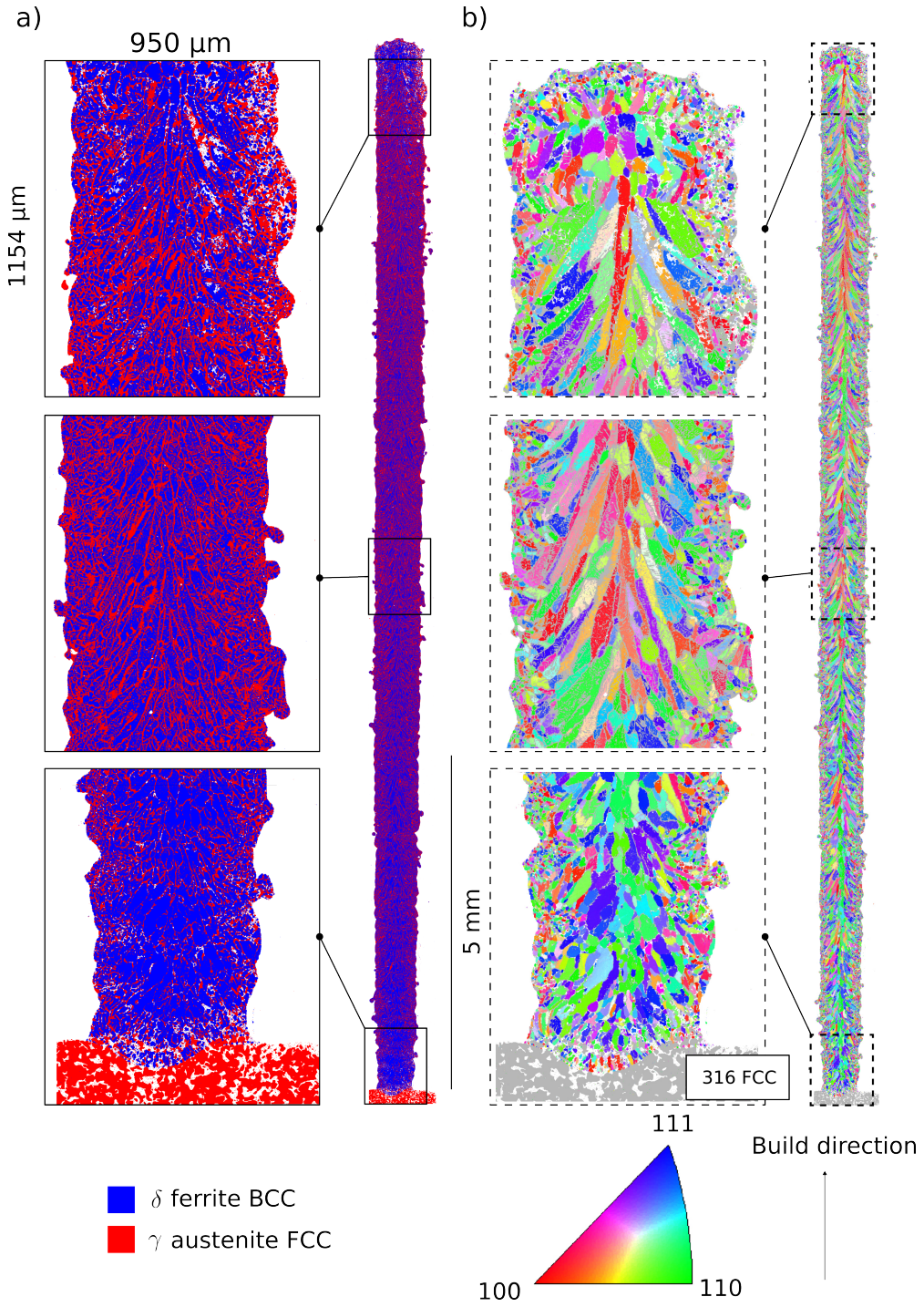


Figure 5: Microstructure of the cross-section for 250 W laser power: a) EBSD phase map b) inverse pole figure map.

the original ferrite grain size is relatively difficult due to the presence of a high fraction of austenite. The phase map in figure 5 (a) shows how the austenite grows in the matrix of ferrite mostly along

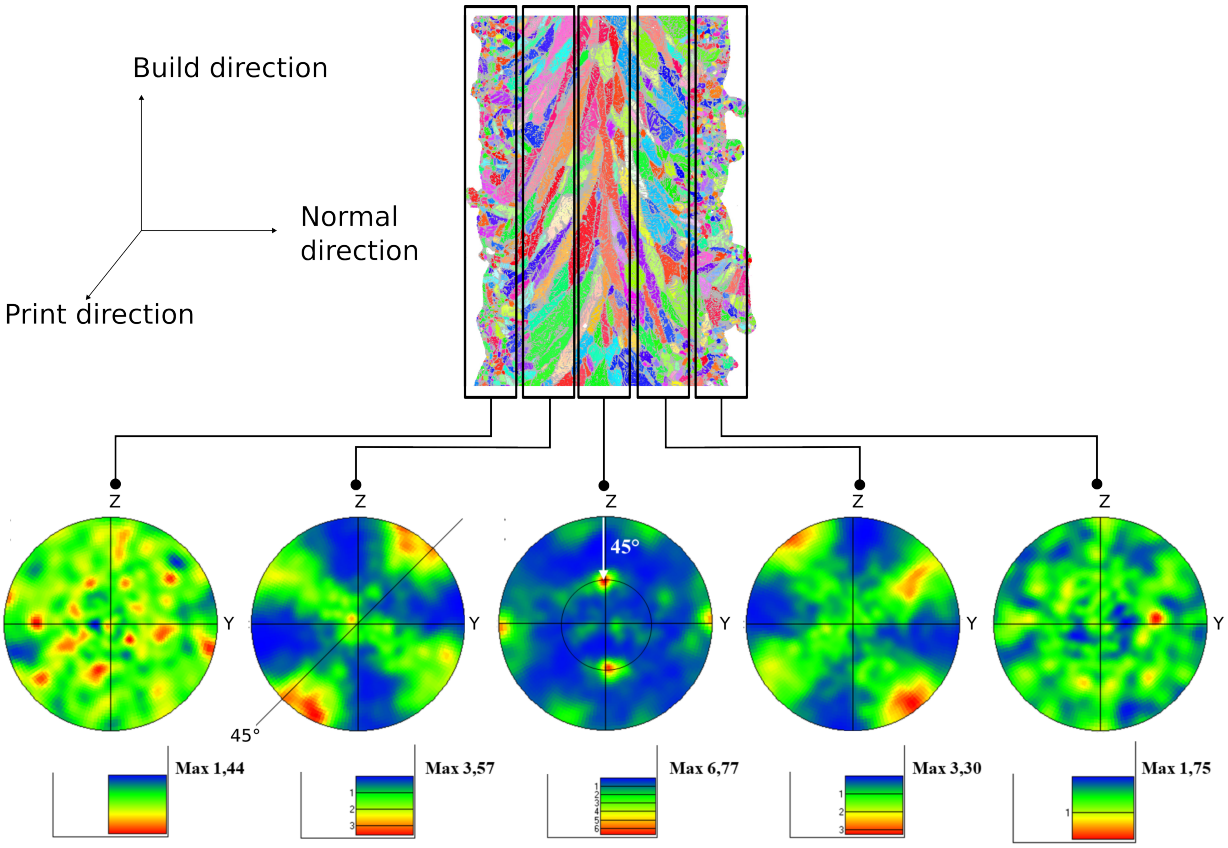


Figure 6: [100] Pole figures of ferrite phase giving the textures of AM wall as a function of depth from the wall surface, 250 W

the prior ferrite GBs. For the small equiaxed ferrite grains near the surface, the austenite forms exclusively along the GBs. For larger epitaxial grains, where less grain boundary area is available, the austenite grows also partly into the grains as parallel dendrites.These vary in their spacing, but are generally of the order of 10 µm.

An analysis of austenite phase fraction as a function of distance from the substrate was made in figure 7 by extracting row by row the data from the phase map in figure 5. On this scatter plot, in the initial stages of fabrication, heat can escape quickly through the proximity of the relatively large substrate. This means cooling rates are faster, and less time is spent at high temperatures, limiting austenite growth in these initial DSS layers. As the fabrication progresses, and the layers are printed further from the substrate, the fraction of austenite increases (relatively more *red* phase is visible in figure 5). Finally, the last few layers at the end of the printing process contain less austenite (dip in the curve). There is a lack of subsequent layers reheating the structure, meaning less austenite formed.

### *4.3. Numerical results and comparison with experiments*

Material parameters used in the simulation are detailed. Heat transfer coefficients (HTC) have been estimated in [20] by comparing numerical results and infrared pyrometer measurements.

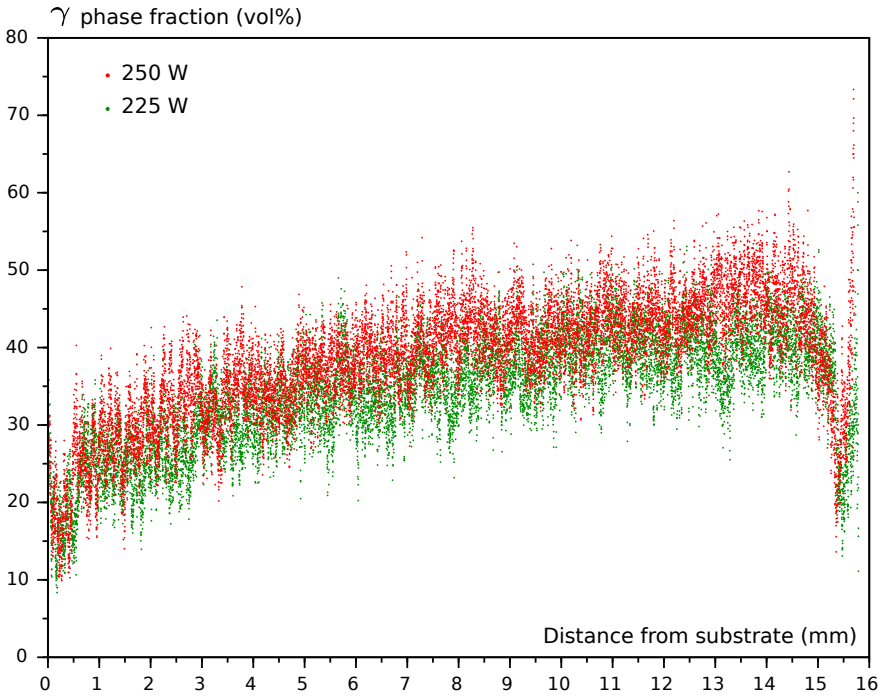


Figure 7: Graph of austenite phase fraction of the duplex printed wall as a function of distance from the substrate

However, the HTC between the build platform and the machine plate underneath has been decreased as the build platform was not clamped to the machine plate therefore decreasing the HTC.

The grain size after solidification should also be estimated. The grain size is computed as a function of the cooling rate (instead of using a single measured value for all the layers) to take into account these opposite effects on phase transition kinetics for heterogeneous cooling rates along the height of the structure. Within the framework of fast simulation a simple empirical approach [37] enables to relate the grain size and the cooling rate during solidification in the form of a power law:

$$R = R_0 \left( \frac{\chi}{\dot{T}_{\text{sol}}} \right)^n \tag{12}$$

Where $\chi$ and $n$ are calibration coefficients, and $\dot{T}_{\text{sol}}$ is the average cooling rate during solidification. This empirical formula has been calibrated for ferritic solidification in [41] for cooling rates ranging from 50 to $10^4$ K.s$^{-1}$. Since for the 2507 duplex steel, the primary solidification is fully ferritic, the estimate reported in [41] (i.e., $R_0$=1 µm, $\chi = 3.2 \times 10^6$ K.s$^{-1}$ and $n = 0.4$) has been used as a basis for the present study. From the EBSD map in figure 5, the average grain radius is roughly estimated to around 10 µm so that the estimate is slightly modified to $\chi = 2.6 \times 10^6$ K.s$^{-1}$.

In addition, thermal properties of 2507 DSS can be estimated as a function of temperature from experimental data as reported in [42]. However, to the best of our knowledge there is no measurement of thermal properties of liquid 2507 DSS. These properties are needed in (1) to estimate the deposition temperature.Thermal conductivity and diffusivity of the liquid phase are chosen as twice the values of the solid state. The resulting value for the thermal diffusivity of the liquid is

consistent with very low specific heat measured at high temperature in [42].

Furthermore, diffusivity coefficients of alloying elements are classically given in the form of Arrhenius laws:

$$D = D_0 \exp\left(-\frac{Q}{\mathrm{R}\,T}\right) \tag{13}$$

Where R (J.mol$^{-1}$.K$^{-1}$) is the gas constant, $D_0$ (m$^2$.s$^{-1}$) the pre-factor and $Q$ (J.mol$^{-1}$) the activation energy. Pre-exponential factors and activation energies are extracted from the literature. Diffusion properties of N in the $\delta$ and $\gamma$ phases of a DSS have been measured between 350 to 500 °C in [43] and at 1200 °C in [44]. A fit of (13) on these data gives $D_0 = 2 \times 10^{-6}$ m$^2$.s$^{-1}$ and $Q = 117000$ J.mol$^{-1}$, and are assumed to be identical in both $\delta$ and $\gamma$ phases. Furthermore, diffusion properties of Ni have been collected in [45] for various Cr-Fe-Ni alloys, and a parametric formula has been fitted on the experimental data. Using this fitted formula and chemical composition in table 1 one obtains for Ni diffusion parameters: $D_0 = 420 \times 10^{-6}$ m$^2$.s$^{-1}$ and $Q = 218000$ J.mol$^{-1}$ assumed to be identical for both $\delta$ and $\gamma$ phases. All material properties used in the proposed simulation are listed in table 3.

Table 3: Material parameters

| | | | |
|---|---|---|---|
| Liquidus temperature | $T_{\mathrm{liq}}$ | (K) | 1738 |
| Solidus temperature | $T_{\mathrm{sol}}$ | (K) | 1677 |
| Powder absorptivity | $\eta$ | (-) | 0.3 |
| Thermal conductivity of the liquid metal | $\lambda_{\mathrm{liq}}$ | (W.m$^{-1}$.K$^{-1}$) | 30 |
| Thermal diffusivity of the liquid metal | $D_{\mathrm{liq}}$ | (m$^2$.s$^{-1}$) | $13\times10^{-6}$ |
| Specific heat of liquid | $c_{p,\mathrm{liq}}$ | (J.kg$^{-1}$.K$^{-1}$) | 290 |
| Thermal conductivity of the solid metal | $\lambda_{\mathrm{sol}}$ | (W.m$^{-1}$.K$^{-1}$) | 15 |
| Thermal diffusivity of the solid metal | $D_{\mathrm{sol}}$ | (m$^2$.s$^{-1}$) | $6.5\times10^{-6}$ |
| Specific heat of solid | $c_{p,\mathrm{sol}}$ | (J.kg$^{-1}$.K$^{-1}$) | 406 |
| Density | $\rho$ | (kg.m$^{-3}$) | 7830 |
| Latent heat of fusion | $L_f$ | (J.g$^{-1}$) | 300 |
| Pre-exponential factor for N in (13) | $D_0$ | (m$^2$.s$^{-1}$) | $2\times10^{-6}$ |
| Activation energy for N in (13) | $Q$ | (J.mol$^{-1}$) | 11700 |
| Pre-exponential factor for Ni in (13) | $D_0$ | (m$^2$.s$^{-1}$) | $420\times10^{-6}$ |
| Activation energy for Ni in (13) | $Q$ | (J.mol$^{-1}$) | 21800 |
| Reference grain size in (12) | $R_0$ | (µm) | 1 |
| Reference cooling rate in (12) | $\chi$ | (K.s$^{-1}$) | $2.6 \times 10^6$ |
| Exponent in (12) | $n$ | (-) | 0.4 |
| HTC part/air | $H_{\mathrm{air}}$ | (W.m$^{-2}$.K$^{-1}$) | 15 |
| HTC part/build platform | $H_{\mathrm{build}}$ | (W.m$^{-2}$.K$^{-1}$) | 20000 |
| HTC build platform/machine plate | $H_{\mathrm{plate}}$ | (W.m$^{-2}$.K$^{-1}$) | 500 |

The Thermo-Calc computation provides the equilibrium concentrations of the different alloying elements involved in the diffusion problem, which are presented in figure 8.

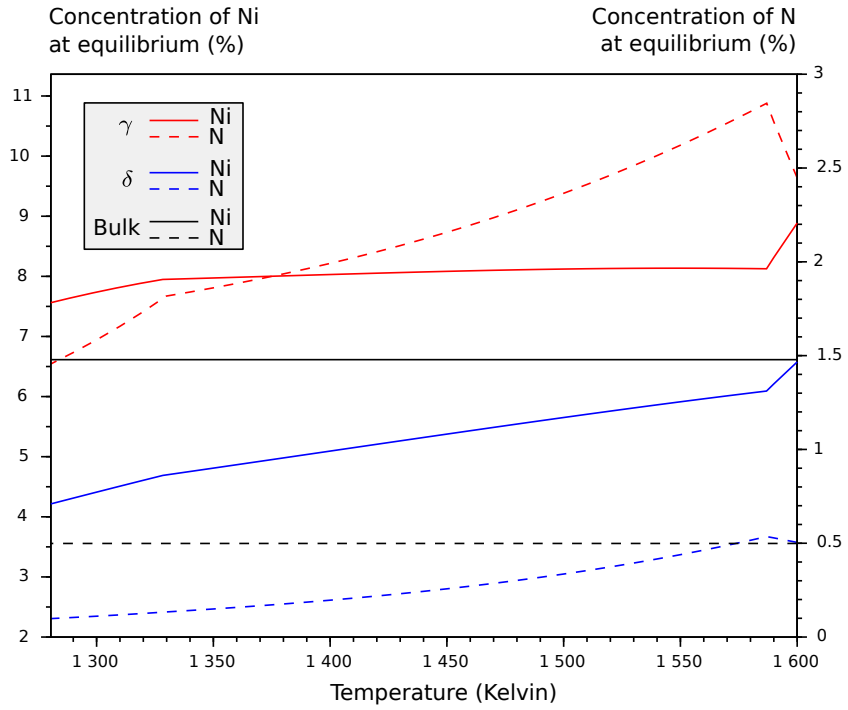


Figure 8: Equilibrium concentration of Ni and N in mol%.

The proposed thermal analysis and phase transition model are applied and compared to the tested experimental conditions. The temperature history can be extracted at any location in each layer. In this study to avoid to deal with large amounts of data, only the middle of each layer is considered at the location where the samples have been extracted. The temperature kinetics of the 1-st layer is presented in figure 9 for both tested conditions (i.e., 225 and 250 W laser power). Temperature cycles clearly show that the temperature range where the $\delta \rightarrow \gamma$ phase transition occur is reached several times. Diffusion profiles of Ni are presented in figure 10 for the first layer at different times in order to understand the diffusion mechanisms. The initial $\gamma$ layer is fixed to 5% of the total cell size $R$ in order to avoid extremely thin time discretization if nearly zero thickness were chosen. (Several computations with different initial thicknesses show that 5% leads to similar results with much coarser time discretization than smaller initial austenite thicknesses). As already mentioned, the initial Ni concentration is uniform and equal to the bulk concentration 6.61mol% (i.e., 7wt%) as listed in table 1. When the phase transition is assisted by N diffusion (i.e., red dot lines in figure 10), Ni atoms diffuse from ferrite to austenite as the equilibrium concentration in the $\gamma$ side $c^{\gamma}_{\text{eq}}$ is larger than the initial bulk concentration. As a result, when the phase transition starts to be limited by Ni diffusion (i.e., red solid lines in figure 10), the Ni concentration in the austenite layer is around 8 to 8.5mol%, although the equilibrium concentration $c^{\gamma}_{\text{eq}}$ decreases. This results in an additional driving force to move the $\delta/\gamma$ interface in the direction of austenite thickening, as detailed in (10). In the $\delta$ side, when the phase transition is assisted either by N diffusion or by

Ni diffusion (i.e., blue dot and solid lines in figure 10), the equilibrium concentration of Ni $c_{\mathrm{eq}}^{\delta}$ is lower than the initial bulk concentration, resulting in a driving force to move the $\delta/\gamma$ interface in the direction of the austenite thickening.

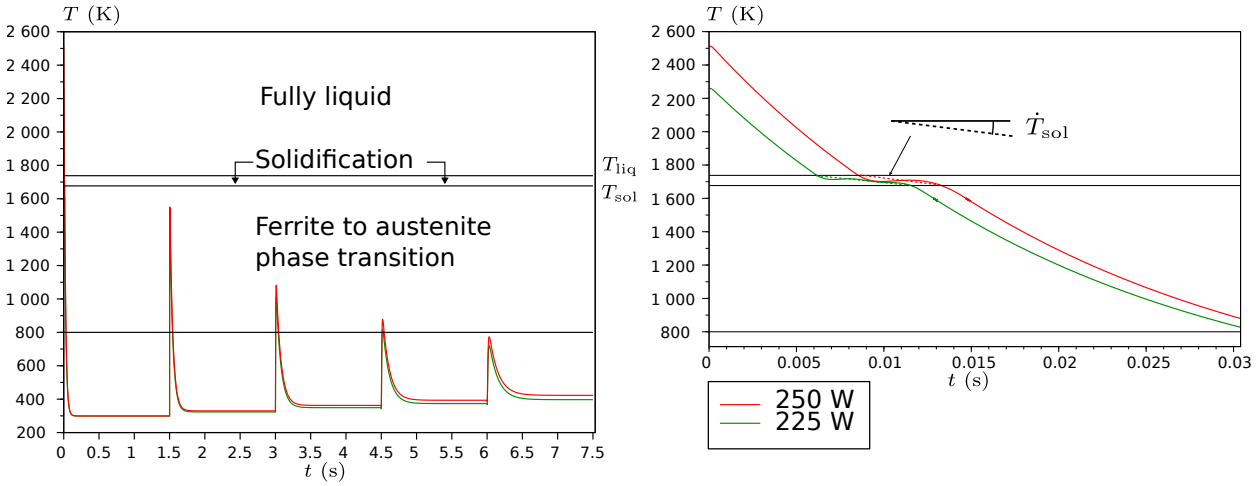


Figure 9: Computed temperature cycles (left) and magnification (right) (1st layer, 250 W and 225 W).

A comparison between measured and computed $\gamma$ phase fraction is presented in figure 11 as a function of the position with respect to the build platform, where raw data presented in figure 7 have been averaged to obtain a single value by layer as for the computation. A reasonable agreement is observed for both the experiments corresponding to different laser powers (i.e., 225 and 250 W). Lower power results in lower melt pool temperature and higher cooling rates, which tend to reduce the amount of the product $\gamma$ phase. However, this effect is mitigated by the fact that higher cooling rates leads to finer grain structure, which promote faster phase transition. This explains the fact that the difference between the measured phase fractions of both experiments is relatively small.

Heterogeneous phase fraction profiles are obtained according to the history of the temperature field. The first layers cool down faster because of the influence of the build platform acting as heat sink and resulting in lower $\gamma$ phase fractions. Cooling rates decrease with the distance to the build platform because the melt pool is further and further from the heat sink whose temperature increases with time. This structural effect tends to a nearly steady state after more than half of the total number of layers in the tested conditions.

Furthermore, the last few layers undergo less thermal cycling than previous layers due to the interruption of fabrication, which results in a significant decrease of the transformed phase fraction. Indeed, thermal cycling plays a significant role as shown in figure 12.

## 5. Numerical investigation for controlling phase distribution

In section 4.3 the influence of laser power, other things being equal, has been demonstrated. In this section, the effect of controlling the substrate temperature on the phase transition distribution is numerically investigated in order to reach a more uniform and balanced $\delta/\gamma$ phase ratio. Excepted

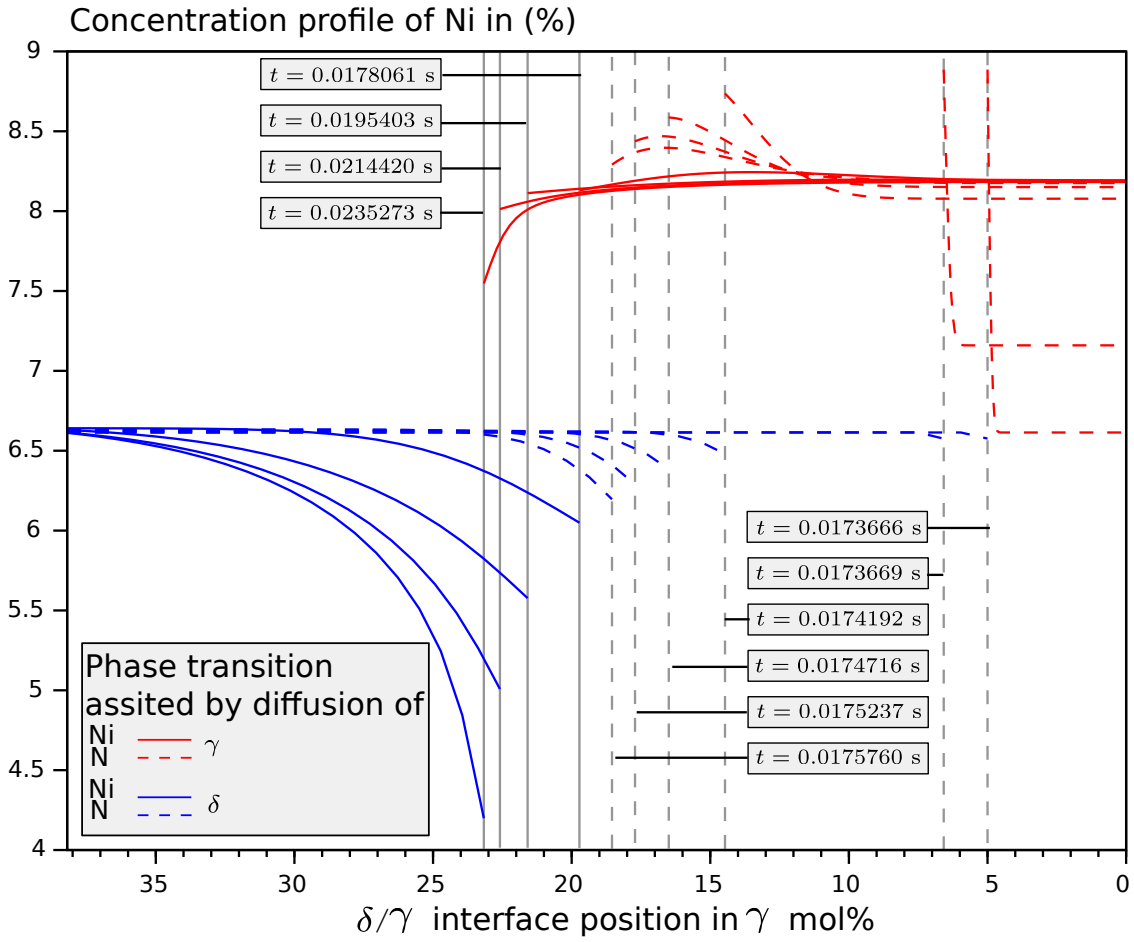


Figure 10: $\delta/\gamma$ interface and Ni concentration profile in mol% at different times when phase transition is assisted by N and Ni diffusion respectively (1st layer, 250 W).

for the tested parameter all process parameters are identical to those listed in table 2 (with laser power $P_{\text{beam}}$ set to 250 W).

First the effect of preheating the build platform is investigated. That is to say that the initial temperature of the build platform is prescribed, and then when the fabrication starts, the heating device is shut down so that the build platform temperature naturally evolves with the laser input.

Three different initial build platform temperatures have been tested (300 K, which is the reference computation without preheating, 600 K and 800 K). Resulting $\gamma$ phase fraction profiles are presented in figure 13. Increasing the pre-heating of the build platform, from 300 K (reference), to 600 K or 800 K results in a corresponding relative increase in austenite phase fraction. This preheating of the build platform slows cooling rates in the part, this is especially important in the temperature range where N and Ni diffuse fastest, which explains the observed increases in austenite phase fraction. In the second half of the part, as the number of layers increases, the local temperature around the melt pool is less affected by the build platform temperature. This leads to a stabilising of the austenite phase fraction which approaches the fraction of the reference unheated

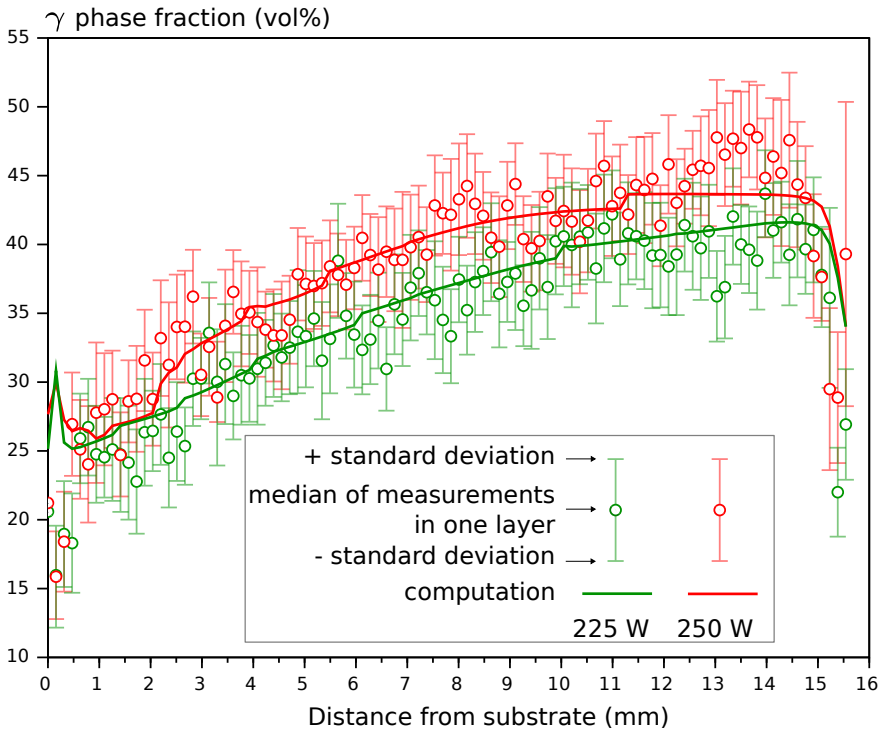


Figure 11: Comparison of measured and computed $\gamma$ phase fraction for 225 and 250 W.

sample (i.e., 300 K). The principal purpose of preheating the substrate is therefore to try to create a more uniform phase fraction in order to match the initial phase fraction with the steady state condition towards the end of the part. In order to reach even more uniform phase fraction distribution in the part, closer to a 50/50 phase ratio, one could imagine a control of the substrate temperature during fabrication using a heating/cooling device with a control loop. The proposed temperature control profile here linearly decreases from 1000 K from the first layer to 800 K by the last layer. This example, as presented in figure 13, shows the most uniform phase fraction distribution of austenite to ferrite across the whole part and nearest to the targeted 50/50 ratio.

Of course this simple analysis does not replace a proper parametric study for each specific part. Indeed there is a complex interweaving between process parameters such as laser power and speed, scanning strategy, dwell time, build platform temperature control etc., and properties of the build such as the deposition temperature (see. equation (1)), layer height and thickness (as reported for instance in [46]), grain size, all having a significant influence on the phase transition kinetics. However, the tools proposed in this contribution enables to reach sufficiently short computation time to be able to optimize the phase fraction ratio in DSS parts.

## 6. Conclusion

In this paper an experimental study enabled to characterise the microstructure (grain morphology and austenite to ferrite ratio) in a super duplex stainless steel (i.e., SAF-2507) obtained by

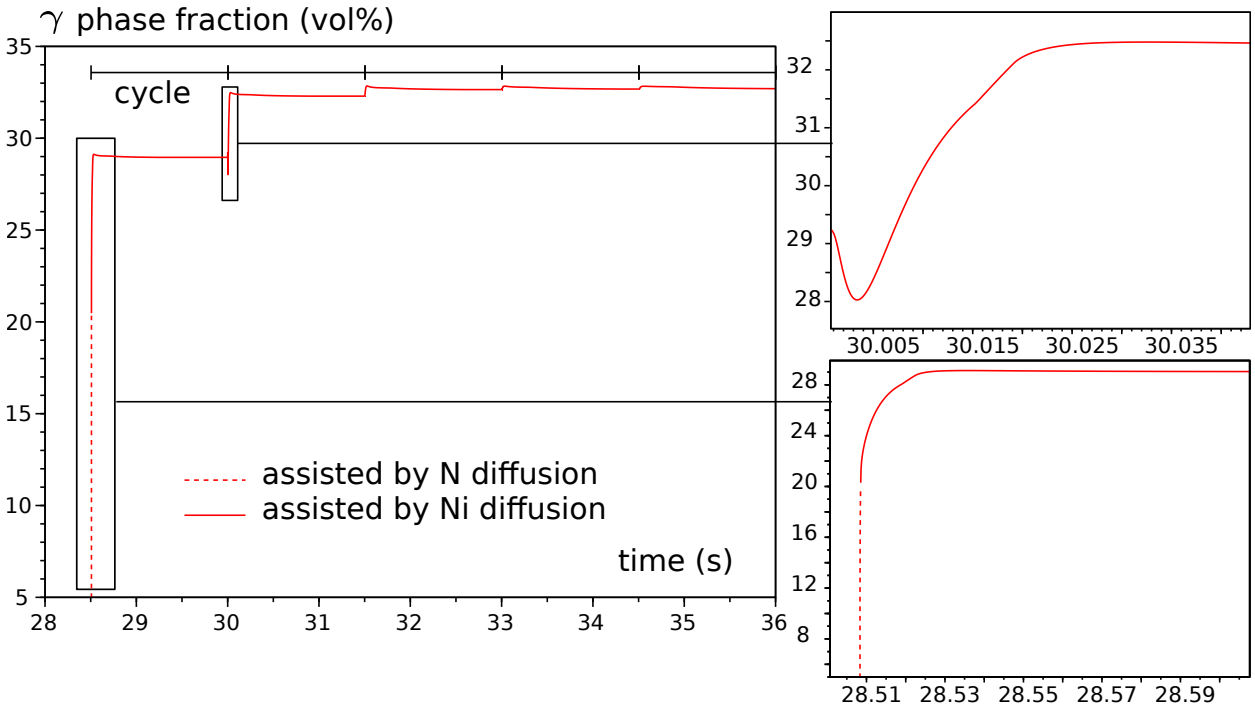


Figure 12: Influence of thermal cycling on phase transition (20-th layer, 250 W).

directed energy deposition additive manufacturing. The thermal history in this fabrication process being rather complex, heterogeneous phase fraction distributions have been observed, and higher power is associated with higher austenite phase fraction. After around 50 layers phase fraction profiles tend to stabilize to a ferrite to austenite phase ratio near 55/45 for 250 W and 60/40 for 225 W.

Since such duplex stainless steel alloys necessitate ferrite to austenite phase ratio near 50/50 in the entire part, a fast numerical approach (temperature and diffusion controlled phase transition) has been developed to optimize process parameters in order to reach a more uniform phase fraction distribution, which necessitated to impose a temperature profile to the build platform linearly decreasing from 1000 K for the first layer to 800 K for the last layer. Numerical results have been compared to the experiments and a reasonable agreement has been observed. In addition, the model has then been tested to determine suitable temperature control of the build platform in order to reach the desired phase fraction distribution. In addition, the proposed simulation tool is sufficiently fast to consider parametric studies or optimization loops in order to facilitate additive manufacturing of super duplex stainless steels and other alloys undergoing diffusion controlled solid state phase transitions.

**Acknowledgement**

This work received funding from the QUADS project of the Agence Innovation Défense (Ministry of army).

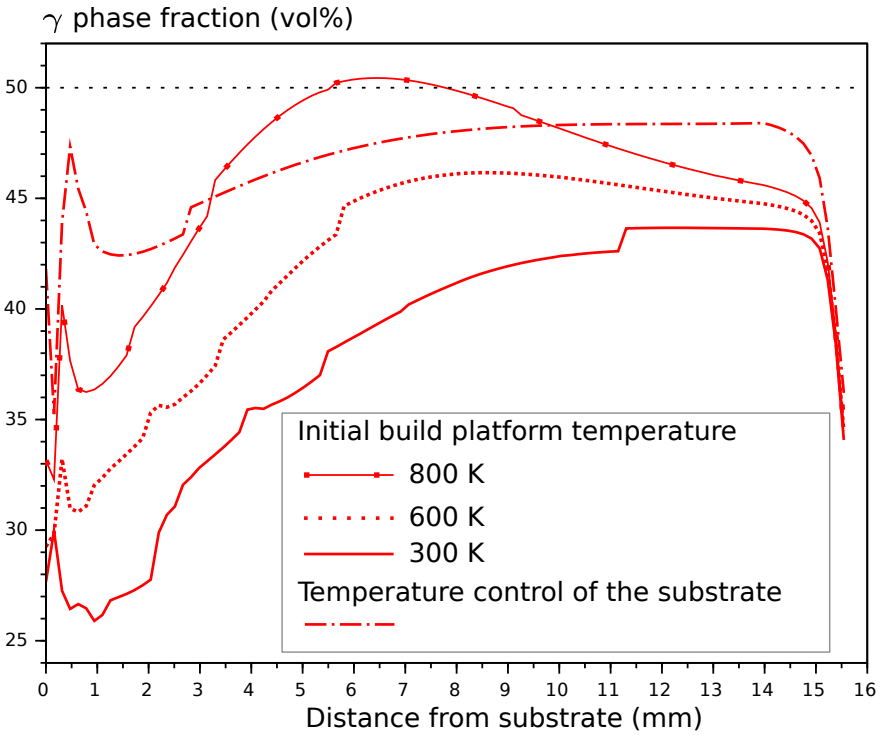


Figure 13: $\gamma$ phase fraction for different initial build platform temperatures and for controlled temperature of the build platform.

## Appendix A. Analytical solution of the substrate temperature

In this section the 1D heat conduction problem (2) with boundary conditions (3) and initial condition (4) is solved analytically. Separation of variables enables to write the solution in the form:

$$T^n_{\text{sub}}(Z,t) = \sum_{j=1}^{N} \left( T^n_j \cos\left(\frac{Z}{Z_j}\right) + \widetilde{T}^n_j \sin\left(\frac{Z}{Z_j}\right) \right) \exp\left(-\frac{D_{\text{sub}}}{Z_j^2} t\right) + T^n_1 \frac{Z}{h_{\text{sub}}} + T^n_0 \tag{A.1}$$

where $T^n_j, T^n_1, T^n_0$ are unknown coefficients to be determined. The boundary conditions (3) combined with (A.1) lead to:

$$\begin{pmatrix} T^n_1 \\ T^n_0 \end{pmatrix} = - \begin{pmatrix} -\left(\frac{\lambda_{\text{sub}}}{h_{\text{sub}}} + \frac{H_{\text{build}}}{2}\right) & -H_{\text{build}} \\ \left(\frac{\lambda_{\text{sub}}}{h_{\text{sub}}} + \frac{H_{\text{plate}}}{2}\right) & -H_{\text{plate}} \end{pmatrix}^{-1} \cdot \begin{pmatrix} H_{\text{build}}\, T^n_{\text{build}} \\ H_{\text{plate}}\, T_{\text{plate}} \end{pmatrix} \tag{A.2}$$

and for all $1 \leq j \leq N$:

$$\begin{pmatrix} A^+_j & -B^+_j \\ A^-_j & B^-_j \end{pmatrix} \cdot \begin{pmatrix} T^n_j \\ \widetilde{T}^n_j \end{pmatrix} = \begin{pmatrix} 0 \\ 0 \end{pmatrix} \tag{A.3}$$

where:

$$\begin{cases} A_j^+ = \dfrac{\lambda_{\text{sub}}}{Z_j}\sin\left(\dfrac{h_{\text{sub}}}{2Z_j}\right) - H_{\text{build}}\cos\left(\dfrac{h_{\text{sub}}}{2Z_j}\right) \\ A_j^- = \dfrac{\lambda_{\text{sub}}}{Z_j}\sin\left(\dfrac{h_{\text{sub}}}{2Z_j}\right) - H_{\text{plate}}\cos\left(\dfrac{h_{\text{sub}}}{2Z_j}\right) \\ B_j^+ = \dfrac{\lambda_{\text{sub}}}{Z_j}\cos\left(\dfrac{h_{\text{sub}}}{2Z_j}\right) + H_{\text{build}}\sin\left(\dfrac{h_{\text{sub}}}{2Z_j}\right) \\ B_j^- = \dfrac{\lambda_{\text{sub}}}{Z_j}\cos\left(\dfrac{h_{\text{sub}}}{2Z_j}\right) + H_{\text{plate}}\sin\left(\dfrac{h_{\text{sub}}}{2Z_j}\right) \end{cases} \tag{A.4}$$

Therefore, $Z_j$ are defined as successive positive roots of $A_j^+ B_j^- + A_j^- B_j^+ = 0$, and the following relation holds: $\widetilde{T}_j^n = (A_j^+/B_j^+)T_j^n$. Thus the last coefficients to determine are $T_j^n$. The initial condition (4) involves the substrate temperature at the end of the previous layer deposition, which reads:

$$T_{\text{sub}}^{n-1}(Z, t^{n-1}) = \sum_{j=1}^{N} T_j^{n-1} f_j\left(\frac{Z}{Z_j}\right)\exp\left(-\frac{D_{\text{sub}}}{Z_j^2}t^{n-1}\right) + T_1^{n-1}\frac{Z}{h_{\text{sub}}} + T_0^{n-1} \tag{A.5}$$

where following eigenfunctions have been defined:

$$f_j : y \mapsto \left(\cos(y) + \frac{A_j^+}{B_j^+}\sin(y)\right) \tag{A.6}$$

Because of orthogonality of the eigenfunctions $f_j$ with respect to the inner product (A.8) one obtains:

$$T_j = T_j^{n-1}\exp\left(-\frac{D_{\text{sub}}}{Z_j^2}t^{n-1}\right) + \frac{T_1^{n-1} - T_1^n}{h_{\text{sub}}}\frac{\langle Z, f_j\rangle}{\langle f_j, f_j\rangle} + (T_0^{n-1} - T_0^n)\frac{\langle 1, f_j\rangle}{\langle f_j, f_j\rangle} \tag{A.7}$$

where the usual inner product has been defined:

$$\langle f, g\rangle = \int_{-\frac{h_{\text{sub}}}{2}}^{\frac{h_{\text{sub}}}{2}} f(Z)\, g(Z)\mathrm{d}Z \tag{A.8}$$

## Appendix B. Analytical solution of the diffusion problem

In this section the analytical solution of (5) subjected to boundary conditions (6) and initial condition (7) is derived for slabs, cylinders and sphere (i.e., for $q = 0, 1, 2$). The equation is solved by separation of variables and the solution reads:

$$\begin{cases} c_k^\delta(x,t) = \displaystyle\sum_{j=1}^{N} c_{j,k}^\delta\, f\left(\frac{x}{x_{j,k}^\delta}\right)\exp\left(-\frac{D_k^\delta}{\left(x_{j,k}^\delta\right)^2}(t - t_k)\right) + c_{\text{eq},k}^\delta & \text{if} \quad 0 \le x \le R - w_k \\ c_k^\gamma(x,t) = \displaystyle\sum_{j=1}^{N}\left(c_{j,k}^\gamma\, f\left(\frac{x}{x_{j,k}^\gamma}\right) + \widetilde{c}_{j,k}^\gamma\, g\left(\frac{x}{x_{j,k}^\gamma}\right)\right)\exp\left(-\frac{D_k^\gamma}{\left(x_{j,k}^\gamma\right)^2}(t - t_k)\right) + c_{\text{eq},k}^\gamma & \text{if} \quad R - w_k \le x \le R \end{cases} \tag{B.1}$$

where $c^{\delta}_{j,k}, c^{\gamma}_{j,k}, \widetilde{c}^{\gamma}_{j,k}$ are unknown coefficients, $x^{\delta}_{j,k}, x^{\gamma}_{j,k}$ are the eigenvalues to be determined, and $f$ and $g$ are the following eigenfunctions:

| | $q=0$ | $q=1$ | $q=2$ |
|---|---|---|---|
| $f(x)$ | $\cos(x)$ | $J_0(x)$ | $\dfrac{\sin(x)}{x}$ |
| $g(x)$ | $\sin(x)$ | $Y_0(x)$ | $\dfrac{\cos(x)}{x}$ |

(B.2)

where $J_p$ and $Y_p$ denote the $p$-th order Bessel functions of the first and second kind respectively. Eigenvalues $x^{\delta}_{j,k}, x^{\gamma}_{j,k}$ are determined by using boundary conditions (6), which lead to:

$$f\left(\frac{R-w_k}{x^{\delta}_{j,k}}\right)=0 \quad \text{and} \quad \begin{pmatrix} f\left(\dfrac{R-w_k}{x^{\gamma}_{j,k}}\right) & g\left(\dfrac{R-w_k}{x^{\gamma}_{j,k}}\right) \\ f'\left(\dfrac{R}{x^{\gamma}_{j,k}}\right) & g'\left(\dfrac{R}{x^{\gamma}_{j,k}}\right) \end{pmatrix} \cdot \begin{pmatrix} c^{\gamma}_{j,k} \\ \widetilde{c}^{\gamma}_{j,k} \end{pmatrix} = \begin{pmatrix} 0 \\ 0 \end{pmatrix} \tag{B.3}$$

hence non trivial solution are obtained by computing the roots of the matrix determinant in (B.3):

$$f\left(\frac{R-w_k}{x^{\gamma}_{j,k}}\right) g'\left(\frac{R}{x^{\gamma}_{j,k}}\right) - f'\left(\frac{R}{x^{\gamma}_{j,k}}\right) g\left(\frac{R-w_k}{x^{\gamma}_{j,k}}\right) = 0 \tag{B.4}$$

and:

$$\widetilde{c}^{\gamma}_{j,k} = -\frac{f\left(\frac{R-w_k}{x^{\gamma}_{j,k}}\right)}{g\left(\frac{R-w_k}{x^{\gamma}_{j,k}}\right)} c^{\gamma}_{j,k} \tag{B.5}$$

Therefore the eigenvalues read:

| | $q=0$ | $q=1$ | $q=2$ |
|---|---|---|---|
| $x^{\delta}_{j,k}$ | $\dfrac{R-w_k}{\frac{\pi}{2}+j\,\pi}$ | $\dfrac{R-w_k}{\zeta_j}$ | $\dfrac{R-w_k}{j\,\pi}$ |
| $x^{\gamma}_{j,k}$ | $\dfrac{w_k}{\frac{\pi}{2}+j\,\pi}$ | $\dfrac{w_k}{\xi_j}$ | $\dfrac{w_k}{\chi_{j,k}}$ |

(B.6)

where $\zeta_j$ $(1 \leq j \leq N)$ are the positive successive zero of the 0-order Bessel function of the first kind $J_0$, which are known, $\chi_{j,k}$ are the positive successive roots of $\chi \mapsto (\chi - (w_k/R)\tan(\chi))$, and $\xi_{j,k}$ are the positive successive roots of $\xi \mapsto T_1(R/w_k\,\xi) - T_0((R/w_k - 1)\,\xi)$ (where $T_p = J_p/Y_p$). Therefore, it is clear from (B.6) that the eigenvalues $x^{\delta}_{j,k}$ are fairly easy to compute for each time step $k$ as explicit formulae have been obtained. However, for $q = 1, 2$ the eigenvalues $x^{\gamma}_{j,k}$ necessitate to numerically solve non-linear equations that depend on the time step $k$. Thus, the computation cost is much higher if there is a large number of time steps. Fortunately for slabs (i.e., $q = 0$) the eigenvalues $x^{\gamma}_{j,k}$ are also given explicitly, which enables to reach very short computation times.

Unknown coefficients $c^{\delta}_{j,k}, c^{\gamma}_{j,k}, \widetilde{c}^{\gamma}_{j,k}$ are determined by applying the initial condition (7). Considering the following orthogonality relations:

$$\begin{cases} \left\langle f\left(x/x^{\delta}_{i,k}\right), f\left(x/x^{\delta}_{j,k}\right)\right\rangle^{\delta}_{k} = \begin{cases} 0 & \text{if} \quad i \neq j \\ \neq 0 & \text{if} \quad i = j \end{cases} \\ \left\langle f\left(x/x^{\gamma}_{i,k}\right), f\left(x/x^{\gamma}_{j,k}\right)\right\rangle^{\gamma}_{k} = \begin{cases} 0 & \text{if} \quad i \neq j \\ \neq 0 & \text{if} \quad i = j \end{cases} \\ \left\langle g\left(x/x^{\gamma}_{i,k}\right), g\left(x/x^{\gamma}_{j,k}\right)\right\rangle^{\gamma}_{k} = \begin{cases} 0 & \text{if} \quad i \neq j \\ \neq 0 & \text{if} \quad i = j \end{cases} \\ \left\langle f\left(x/x^{\gamma}_{i,k}\right), g\left(x/x^{\gamma}_{j,k}\right)\right\rangle^{\gamma}_{k} = 0 \end{cases} \tag{B.7}$$

where the inner products are defined as follows:

$$\begin{cases} \langle f_1, f_2\rangle^{\delta}_{k} = \displaystyle\int_{0}^{R-w_k} x^q f_1(x) f_2(x) \mathrm{d}x \\ \langle f_1, f_2\rangle^{\gamma}_{k} = \displaystyle\int_{R-w_k}^{R} x^q f_1(x) f_2(x) \mathrm{d}x \end{cases} \tag{B.8}$$

the coefficients read:

$$\begin{cases} c^{\delta}_{j,k} = \dfrac{\left\langle f(x/x^{\delta}_{j,k}), c^{\delta}_{\mathrm{ini},k}(x)\right\rangle^{\delta}_{k}}{\left\langle f(x/x^{\delta}_{j,k}), f(x/x^{\delta}_{j,k})\right\rangle^{\delta}_{k}} \\ c^{\gamma}_{j,k} = \dfrac{\left\langle f(x/x^{\gamma}_{j,k}), c^{\gamma}_{\mathrm{ini},k}(x)\right\rangle^{\gamma}_{k}}{\left\langle f(x/x^{\gamma}_{j,k}), f(x/x^{\gamma}_{j,k})\right\rangle^{\gamma}_{k}} \\ \widetilde{c}^{\gamma}_{j,k} = \dfrac{\left\langle g(x/x^{\gamma}_{j,k}), c^{\gamma}_{\mathrm{ini},k}(x)\right\rangle^{\gamma}_{k}}{\left\langle g(x/x^{\gamma}_{j,k}), g(x/x^{\gamma}_{j,k})\right\rangle^{\gamma}_{k}} \end{cases} \tag{B.9}$$

Using (8) along with (B.1) it is clear that $c^{\delta}_{\mathrm{ini},k}, c^{\gamma}_{\mathrm{ini},k}$ are given analytically and involves the same eigenfunctions $f$ and $g$, which enables to compute analytically the inner products in (B.9).

The update of the austenite thickness given in (11) reads:

$$\begin{aligned} w_k = w_{k-1} &+ D^{\delta}_{k-1} \sum_{j=1}^{N} c^{\delta}_{j,k}\, f'\left(\frac{x}{x^{\delta}_{j,k}}\right)\left(\frac{x^{\delta}_{j,k}}{D^{\delta}_{k}}\right)\left(1 - \exp\left(-\frac{D^{\delta}_{k}}{\left(x^{\delta}_{j,k}\right)^2}\Delta t_k\right)\right) \\ &- D^{\gamma}_{k-1} \sum_{j=1}^{N} c^{\gamma}_{j,k}\left(f'\left(\frac{x}{x^{\gamma}_{j,k}}\right) - \frac{f\left(\frac{R-w_k}{x^{\gamma}_{j,k}}\right)}{g\left(\frac{R-w_k}{x^{\gamma}_{j,k}}\right)} g'\left(\frac{x}{x^{\gamma}_{j,k}}\right)\right)\left(\frac{x^{\gamma}_{j,k}}{D^{\gamma}_{k}}\right)\left(1 - \exp\left(-\frac{D^{\gamma}_{k}}{\left(x^{\gamma}_{j,k}\right)^2}\Delta t_k\right)\right) \end{aligned} \tag{B.10}$$

## References


[1] J.-S. Lim, W.-J. Oh, C.-M. Lee, D.-H. Kim, Selection of effective manufacturing conditions for directed energy deposition process using machine learning methods, Scientific reports 11 (2021) 1–13.

[2] P. Bajaj, A. Hariharan, A. Kini, P. Kürnsteiner, D. Raabe, E. Jägle, Steels in additive manufacturing: A review of their microstructure and properties, Materials Science and Engineering: A 772 (2020) 138633.

[3] J.-O. Nilsson, Super duplex stainless steels, Materials science and technology 8 (1992) 685–700.

[4] D. Zhang, A. Liu, B. Yin, P. Wen, Additive manufacturing of duplex stainless steels-a critical review, Journal of Manufacturing Processes 73 (2022) 496–517.

[5] F. Hengsbach, P. Koppa, K. Duschik, M. J. Holzweissig, M. Burns, J. Nellesen, W. Tillmann, T. Tröster, K.-P. Hoyer, M. Schaper, Duplex stainless steel fabricated by selective laser melting - Microstructural and mechanical properties, Materials & Design 133 (2017) 136–142.

[6] J. Kunz, A. Boontanom, S. Herzog, P. Suwanpinij, A. Kaletsch, C. Broeckmann, Influence of hot isostatic pressing post-treatment on the microstructure and mechanical behavior of standard and super duplex stainless steel produced by laser powder bed fusion, Materials Science and Engineering: A 794 (2020) 139806.

[7] K. Saeidi, L. Kevetkova, F. Lofaj, Z. Shen, Novel ferritic stainless steel formed by laser melting from duplex stainless steel powder with advanced mechanical properties and high ductility, Materials Science and Engineering: A 665 (2016) 59–65.

[8] M. Brázda, P. Salvetr, J. Dlouhỳ, J. Vavřík, Influence of laser power in direct laser deposition on the proportion of ferrite and austenite in duplex steel saf2507, in: METAL 2020-29th International Conference on Metallurgy and Materials, Conference Proceedings, pp. 539–544.

[9] A. R. Kannan, N. S. Shanmugam, V. Rajkumar, M. Vishnukumar, Insight into the microstructural features and corrosion properties of wire arc additive manufactured super duplex stainless steel (er2594), Materials Letters 270 (2020) 127680.

[10] M. Eriksson, M. Lervåg, C. Sørensen, A. Robertstad, B. M. Brønstad, B. Nyhus, R. Aune, X. Ren, O. M. Akselsen, Additive manufacture of superduplex stainless steel using WAAM, MATEC Web of Conferences 188 (2018) 03014.

[11] A. D. Iams, J. S. Keist, T. A. Palmer, Formation of Austenite in Additively Manufactured and Post-Processed Duplex Stainless Steel Alloys, Metallurgical and Materials Transactions A 51 (2020) 982–999.

[12] Y. Lian, S. Lin, W. Yan, W. K. Liu, G. J. Wagner, A parallelized three-dimensional cellular automaton model for grain growth during additive manufacturing, Computational Mechanics 61 (2018) 543–558.

[13] H. Wei, G. Knapp, T. Mukherjee, T. DebRoy, Three-dimensional grain growth during multi-layer printing of a nickel-based alloy inconel 718, Additive Manufacturing 25 (2019) 448–459.

[14] C. Kumara, A. Segerstark, F. Hanning, N. Dixit, S. Joshi, J. Moverare, P. Nylén, Microstructure modelling of laser metal powder directed energy deposition of alloy 718, Additive Manufacturing 25 (2019) 357–364.

[15] J. Smith, W. Xiong, J. Cao, W. K. Liu, Thermodynamically consistent microstructure prediction of additively manufactured materials, Computational mechanics 57 (2016) 359–370.

[16] D. Zhang, Z. Feng, C. Wang, Z. Liu, D. Dong, Y. Zhou, R. Wu, Modeling of temperature field evolution during multilayered direct laser metal deposition, Journal of Thermal Spray Technology 26 (2017) 831–845.

[17] C. Baykasoglu, O. Akyildiz, D. Candemir, Q. Yang, A. C. To, Predicting microstructure evolution during directed energy deposition additive manufacturing of ti-6al-4v, Journal of Manufacturing Science and Engineering 140 (2018) 051003.

[18] J. Li, Q. Wang, P. P. Michaleris, An analytical computation of temperature field evolved in directed energy deposition, Journal of Manufacturing Science and Engineering 140 (2018) 101004.

[19] C. Guévenoux, M. Nasiry, S. Durbecq, A. Charles, E. Charkaluk, A. Constantinescu, Thermal modeling of ded repair process for slender panels by a 2d semi-analytic approach (2020).

[20] D. Weisz-Patrault, Fast simulation of temperature and phase transitions in directed energy deposition additive manufacturing, Additive Manufacturing 31 (2020) 100990.

[21] D. Weisz-Patrault, Fast macroscopic thermal analysis for laser metal deposition. Application to multiphase steels, in: Sim-AM 2019: II International Conference on Simulation for Additive Manufacturing, CIMNE, pp. 60–71.

[22] D. Weisz-Patrault, P. Margerit, A. Constantinescu, Residual stresses in thin walled-structures manufactured by

directed energy deposition: In-situ measurements, fast thermo-mechanical simulation and buckling, Additive Manufacturing (2022) 102903.
[23] D. Weisz-Patrault, S. Sakout, A. Ehrlacher, Fast simulation of temperature and grain growth in directed energy depostion additive manufacturing, in: 14th World Congress on Computational Mechanics, volume 1, ECCOMAS Congress, p. 2748.
[24] S. Sakout, D. Weisz-Patrault, A. Ehrlacher, Energetic upscaling strategy for grain growth. I: Fast mesoscopic model based on dissipation, Acta Materialia 196 (2020) 261–279.
[25] D. Weisz-Patrault, S. Sakout, A. Ehrlacher, Energetic upscaling strategy for grain growth. II: Probabilistic macroscopic model identified by Bayesian techniques, Acta Materialia (2021).
[26] A. Miodownik, N. Saunders, Modelling of materials properties in duplex stainless steels, Materials Science and Technology 18 (2002) 861–868.
[27] T. Berecz, É. Fazakas, I. Mészáros, I. Sajó, Decomposition kinetics of ferrite in isothermally aged saf 2507-type duplex stainless steel, Journal of Materials Engineering and Performance 24 (2015) 4777–4788.
[28] H. K. Bhadeshia, Diffusional formation of ferrite in iron and its alloys, Progress in Materials Science 29 (1985) 321–386.
[29] J. Vitek, S. Vitek, S. David, Numerical modeling of diffusion-controlled phase transformations in ternary systems and application to the ferrite/austenite transformation in the fe-cr-ni system, Metallurgical and Materials Transactions A 26 (1995) 2007–2025.
[30] J. Andersson, L. Höglund, B. Jönsson, J. Ågren, C. Purdy, Fundamentals and applications of ternary diffusion, New York (1990).
[31] S. Wessman, M. Selleby, Evaluation of austenite reformation in duplex stainless steel weld metal using computational thermodynamics, Welding in the World 58 (2014) 217–224.
[32] T. Keller, G. Lindwall, S. Ghosh, L. Ma, B. M. Lane, F. Zhang, U. R. Kattner, E. A. Lass, J. C. Heigel, Y. Idell, et al., Application of finite element, phase-field, and calphad-based methods to additive manufacturing of ni-based superalloys, Acta materialia 139 (2017) 244–253.
[33] K. Teferra, D. J. Rowenhorst, Optimizing the cellular automata finite element model for additive manufacturing to simulate large microstructures, Acta Materialia 213 (2021) 116930.
[34] S. Liu, Y. C. Shin, Integrated 2d cellular automata-phase field modeling of solidification and microstructure evolution during additive manufacturing of ti6al4v, Computational Materials Science 183 (2020) 109889.
[35] A. Prasad, L. Yuan, P. Lee, M. Patel, D. Qiu, M. Easton, D. StJohn, Towards understanding grain nucleation under additive manufacturing solidification conditions, Acta Materialia 195 (2020) 392–403.
[36] T. Quested, A. Greer, Grain refinement of al alloys: Mechanisms determining as-cast grain size in directional solidification, Acta Materialia 53 (2005) 4643–4653.
[37] M. C. Flemings, Solidification processing, Metallurgical and Materials Transactions B 5 (1974) 2121–2134.
[38] J.-O. Andersson, T. Helander, L. Höglund, P. Shi, B. Sundman, Thermo-calc & dictra, computational tools for materials science, Calphad 26 (2002) 273–312.
[39] D. Bäuerle, Laser processing and chemistry, Springer Science & Business Media, 2013.
[40] C. Herrera, N. De Lima, A. Kliauga, A. Padilha, Microstructure and texture of duplex stainless steel after melt-spinning processing, Materials Characterization 59 (2008) 79–83.
[41] N. Pryds, X. Huang, The effect of cooling rate on the microstructures formed during solidification of ferritic steel, Metallurgical and Materials Transactions A 31 (2000) 3155–3166.
[42] R. H. A. Abas, N. K. Taieh, Experimental study of the thermal diffusivity and heat capacity concerning some duplex stainless steel, Al-Khwarizmi Engineering Journal 11 (2015) 51–61.
[43] M. Bobadilla, A. Tschiptschin, On the nitrogen diffusion in a duplex stainless steel, Materials Research 18 (2015) 390–394.
[44] R. Zhou, D. O. Northwood, C. Liu, On nitrogen diffusion during solution treatment in a high nitrogen austenitic stainless steel, Journal of Materials Research and Technology 9 (2020) 2331–2337.
[45] B. Jönsson, Assessment of the mobilities of cr, fe and ni in bcc cr-fe-ni alloys, ISIJ international 35 (1995) 1415–1421.
[46] M. Bréhier, D. Weisz-Patrault, C. Tournier, Revisiting the influence of the scanning speed on surface topography and microstructure of in718 thin walls in directed energy deposition additive manufacturing, Procedia CIRP 108

(2022) 470–476.